# Potential megathrust co-seismic slip during the 2020 Sand Point, Alaska strike-slip earthquake

Sean R. Santellanes[1], Diego Melgar[1], Brendan W. Crowell[2], Jiun-Ting Lin[1]

[1]Department of Earth Sciences, University of Oregon
[2]Department of Earth and Space Sciences, University of Washington

***Abstract***
On October 2020, a Mw 7.6 earthquake struck to the south of the Shumagin Islands in Alaska, nearly 3 months after the Mw 7.8 Simeonof megathrust event. The initial models of the earthquake indicated a largely strike-slip rupture; however, the observed tsunami was much larger and widespread than expected for the focal mechanism. We investigate what sea surface deformation is necessary to recreate the tsunami waveforms using water-level inversion techniques. We find that the sea surface deformation does not resemble that expected from a purely strike-slip earthquake. We then carry out slip inversions with water level and static GNSS data as input. We explore the likelihood of megathrust co-seismic slip aiding tsunamigenesis. We propose that, concurrently with strike-slip faulting, it is likely that a considerable slip occurred on the megathrust westward and updip from the previous July 2020 event. We also propose that a smaller submarine landslide is likely to have occurred in an area prone to them. The Sand Point earthquake potentially released ~2 meters of accumulated slip in the western Shumagin Gap, but likely did not slip updip of ~15 km depth.

***Plain Language Summary***
Strike-slip earthquakes often are not a cause for worry when it comes to tsunami hazards. They usually produce negligible amounts of uplift and subsidence on the seafloor. However, a magnitude 7.6 earthquake seemingly did the impossible and caused a hazardous (coastal amplitudes >30 cm) tsunami in Alaska and Hawai'i. We gauge how the earthquake was able to do so by looking at water-level data from tide gauges and open ocean buoys as well as with GNSS data. We find that the strike-slip earthquake had help from potentially megathrust co-seismic activity and a submarine landslide in creating the tsunami.

# 1. Motivation

Tsunamis are most often the result of earthquake sources at subduction zones. Megathrust co-seismic slip is a key process for tsunamigenesis as it typically produces vertical coseismic motion which leads to sea surface deformations large enough to result in hazardous waves (coastal amplitudes > 30cm). The Shumagin segment of the Alaskan Subduction Zone (Figure 1) has been characterized as an area that has largely been devoid of great earthquakes (Mw >= 8.0) for at least the past 100 years (Davies et al, 1981). This may be due to it being in transition between the fully creeping Sanak segment to the west and fully locked Semedi segment to its east (Li & Freymueller, 2018). The Shumagin segment is different with respect to its neighboring segments; great earthquakes have been observed in the Sanak segment (Mw 8.6,

1946) and the Semedi segment (Mw 8.3, 1938) (Davies et al., 1981; Li & Freymueller, 2018; Witter et al., 2014). These have been shown to have produced large, devastating tsunamis from megathrust co-seismic slip. The last known great earthquake in the Shumagin segment is commonly thought to have occurred in 1788; however, geologic observations point that two large earthquakes occurring in just over a month between each other would be more consistent with those observations (Witter et al., 2014).

On 22 July, 2020, the Mw 7.8 ($M_0$=6.91x$10^{20}$ N-m) Simeonof earthquake occurred on the megathrust portion near Simeonof Island (Figure 1, Crowell & Melgar, 2020), producing a small tsunami (Liu et al., 2021; Larson et al., 2021) with ~30cm maximum amplitude at the nearby Sand Point, AK tide gauge (amplitude measured relative from normal sea level). The tsunami had small amplitudes (< 1cm) in the open ocean buoys in the surrounding area. In stark contrast to this, the 19 October, 2020 Mw 7.6 ($M_0$ = 2.82x$10^{20}$ N-m) Sand Point earthquake produced a tsunami with maximum amplitude of 76 cm at the same Sand Point tide gauge, and a ~0.30 cm maximum amplitude at the Hilo, Hawai'i tide gauge, more than 3800 km away. This despite the epicentral region of the two events being the same. It was also recorded clearly by 4 open ocean buoys, as seen in Figure 1. The focal mechanism of this earthquake according to the U.S Geological Survey's (USGS) W-Phase solution was a 49° westward-dipping strike-slip fault (Figure 1) with a 71% double-couple component. The shaking reached Modified Mercalli Intensity (MMI) VII for both events. How the Sand Point event was able to produce a significantly larger local and trans-oceanic tsunami given it is ~2.5 times smaller, by scalar moment, than the Simeonof event and that it has a strike-slip focal mechanism is not clearly understood. It has been generally accepted that strike-slip earthquakes do not produce large enough amounts of vertical sea surface deformation necessary to generate tsunamis with amplitudes > 30 cm in the near- or far-field. The peculiar nature of the Sand Point earthquake's tsunami was highlighted again by the 2021 Mw 8.18 ($M_0$ = 2.36x$10^{21}$ N-m) Chignik earthquake (Figure 1), another low-angle thrust which also failed to produce a sizable tsunami. That event had amplitudes of 15.2 cm at the Sand Point tide gauge. Again, the Sand Point earthquake was a full order of magnitude smaller than Chignik by scalar moment, yet it still has somehow produced the largest tsunami of the three-event sequence.

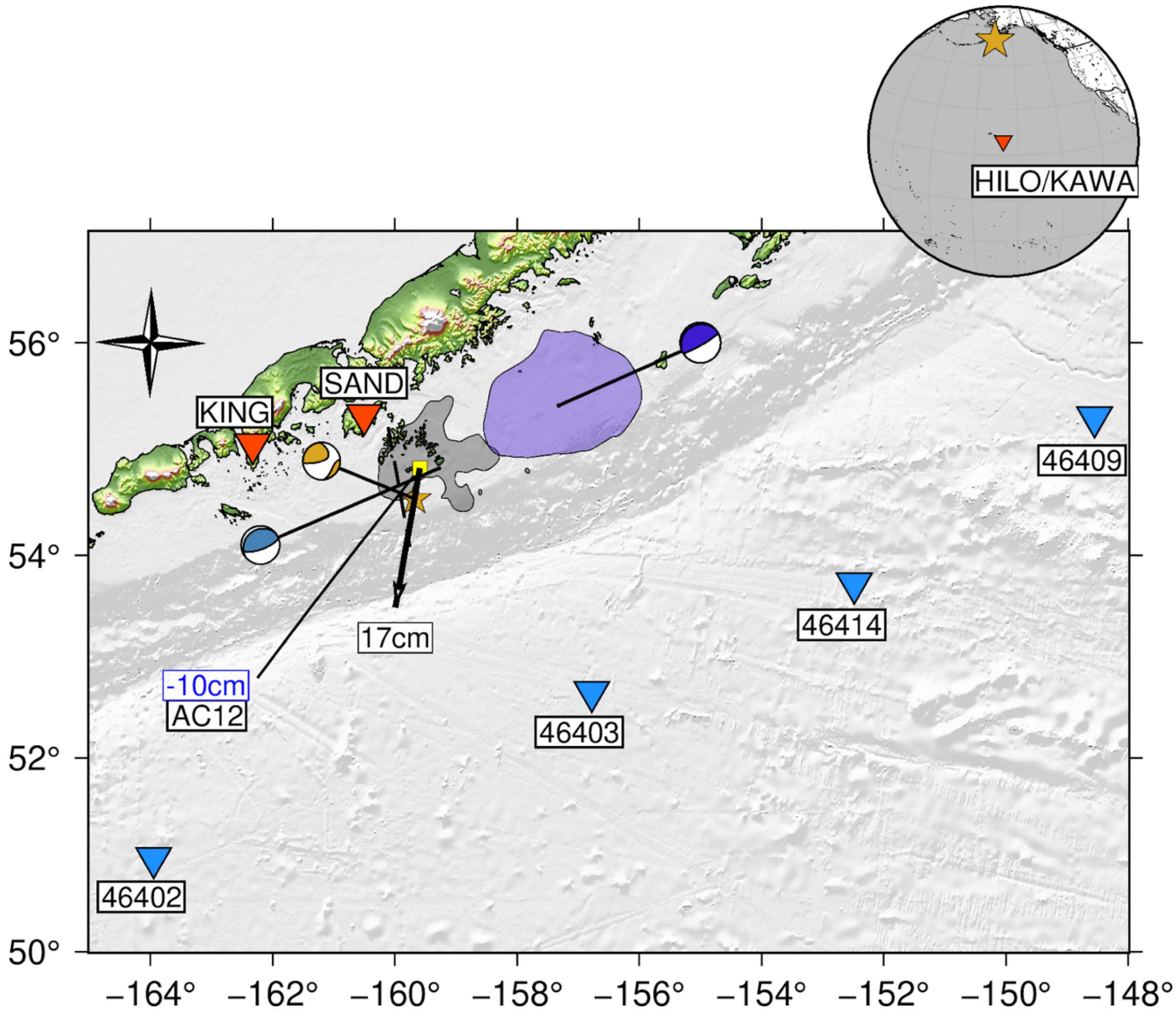


*Fig 1. The study area. The Simeonof rupture zone from Crowell & Melgar (2020) is shown in black, and the Chignik rupture zone from the USGS-NEIC finite fault model for the event is shown in blue. The surface projection of the W-phase moment tensor nodal plane for the Sand Point earthquake is delineated by a dashed black line. The King cove (KING) and Sand Point (SAND) tide gauges are shown in orange-red. DART buoys are shown in dodger-blue. The amount of subsidence at GNSS station AC12 (yellow square) is shown to be -10 cm. The black arrow shows the direction and magnitude of the horizontal vector. The inset shows the locations of the tide gauges in Hawai'i. The gold star denotes the hypocenter of the Sand Point earthquake.*

To unravel what causes co-seismic tsunamis, a common approach is to use finite fault models. Once these are known, they can be used to derive the deformation of the seafloor and use that as a tsunami initial condition. However, as we will show here, the tele-seismic finite fault model from the National Earthquake Information Center (NEIC) does not reproduce either the timing of arrivals or the amplitudes of the tsunami signals at the Alaskan and Hawaiian tide gauges, or the open ocean buoys (Figure 2).

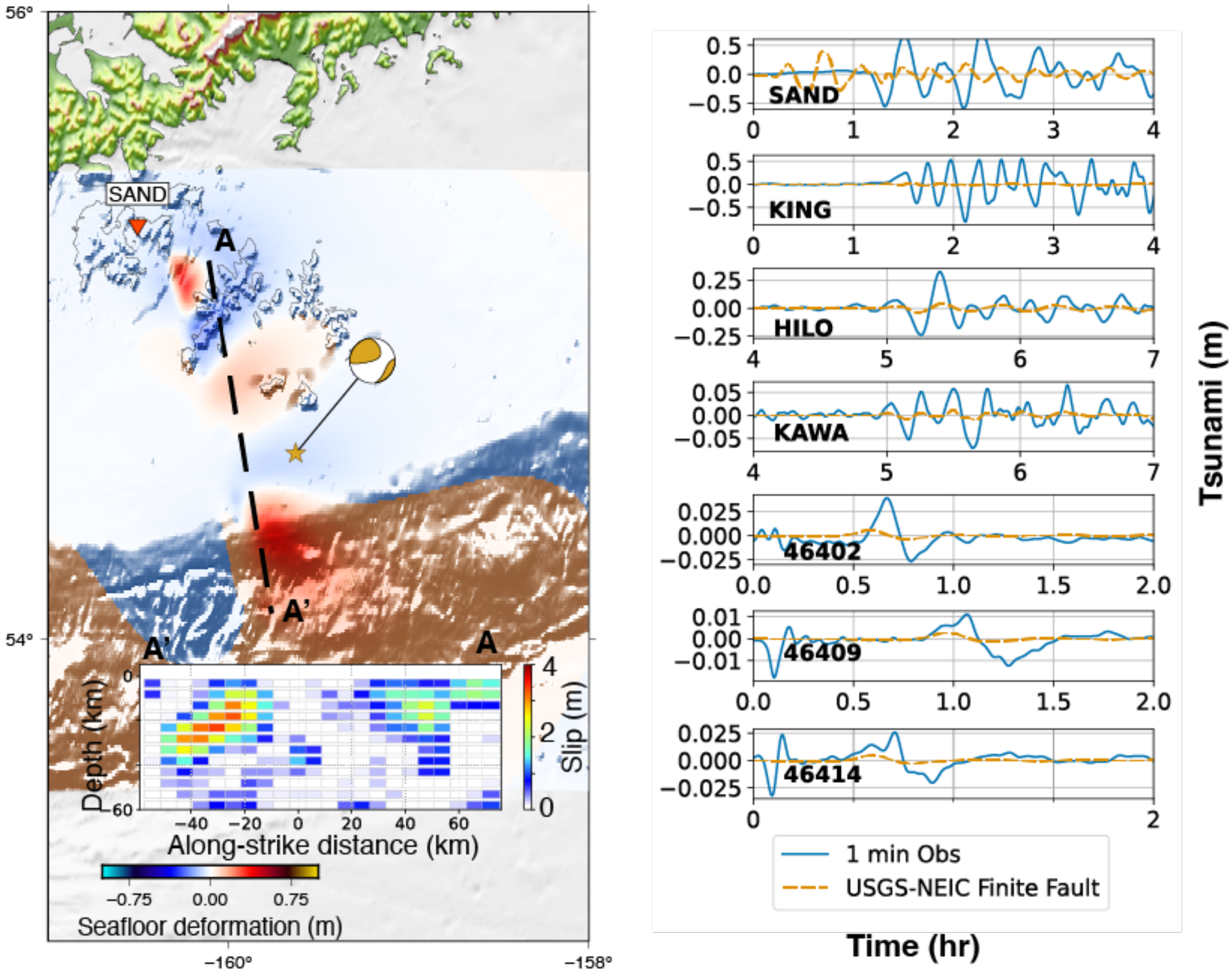


*Figure 2. The USGS-NEIC finite fault model for the Sand Point earthquake and the vertical coseismic deformation resulting from it are shown on the left. The dashed black line from A-A' is the surface projection of the fault plane, and a cross-section of the slip distribution is shown. The hypocenter of the event is denoted by the gold star. On the right, The tsunami waveforms are compared between the observations and the USGS-NEIC model results.*

To understand the event we first take an alternate approach. We use the tide gauge and open ocean buoy data to solve directly for a sea surface deformation model that is able to recreate the tsunami signals at all sites. This technique is attractive because it is devoid of any assumptions on what causes the deformation and simply solves directly for the required initial condition. We then use this inferred sea-surface deformation to explore what combination of tectonic sources, if any, could produce such an initial condition. We will attempt to reconcile the tectonic model with the hydrodynamic model. We will show that the sea surface deformation is most consistent with slip on both the strike-slip fault and the neighboring megathrust. The location we propose for the megathrust slip is just updip of the 2020 M7.8 Simeonof earthquake but stops at 15 km depth; it most likely does not extend to the trench. We also find that to explain the data, especially at the King Cove tide gauge,  a submarine landslide may be necessary.

# 2. Data & Methods

## 2.1 Data & Modeling

The Mw 7.6 Sand Point tsunami was observed by several water-level measuring stations. Here we rely on two near-field tide gauges in the Aleutian Islands, two far-field tide gauges on the island of Hawai'i and four Deep-ocean Assessment And Reporting of Tsunamis (DART) buoys (Figure 1) (Titov et al., 2005). We also use coseismic deformation measured by one Global Navigation Satellite System (GNSS) site, AC12 and processed by the University of Nevada Reno (Blewitt et al., 2018). The bulk of our analysis and subsequent inversion methods are anchored around the water-level data while AC12 provides a constraint on the inferred deformation on land for the inversion methods, with ~10 cm of subsidence and 17 cm of south-south-westward directed displacement. The tide gauges utilized in the inversion have a sampling rate of 1 min, and the DART buoys, in event mode, have a sampling rate between 15 sec and 1 min. We de-tide the water-level data of the observations and models with a bandpass filter between 2 min-120 min for the tide gauges and 15 min to 120 min for the DART buoys. Additionally, to correct the far-field travel time error introduced by unmodeled effects from a compressible seafloor (Tsai et al., 2012), we apply a simple cross-correlation to shift the synthetic data at Hilo.

For the tsunami Green's functions needed by the inversion, and for subsequent, more detailed modeling, we use the open source GeoClaw code (LeVeque et al., 2011). It solves the non-linear shallow-water equations using adaptive mesh refinement so that areas of high tsunami complexity, such as the case with tide gauge locations, can be refined to higher discretization levels. We use SRTM15 (450m pixels) for the model domain in Figure 1. We also use ⅓ arcsec (~10 m pixels) bathymetry/topography to provide greater detail for the areas around the tide gauges. The tsunami simulations are run at 4 levels of mesh refinement starting at 5 arcmin (~7.5 km) and ending at 3 arcsecs (~90 m). Output is collected at the locations of the real world tide gauges and DART buoys.

For the modeling of the fault rupture by the strike-slip geometry, we use the north west striking nodal plane from the USGS W-phase moment tensor solution which is also used in the USGS finite fault model. For the modeling of the megathrust geometry, we use the Slab2 model from Hayes et al. (2018). In addition, we use the crustal velocity model from Pasyanos et al. (2014) when calculating the static Green's functions. We test three different slip inversions, two where the strike-slip and megathrust geometries are run separately and one where they are allowed to slip jointly. Here we only show the results for the strike-slip only and joint models since a strike-slip geometry is required to be consistent with the tele-seismic data.

In addition to the water-level data, when we compute the slip inversion of the strike-slip and/or the joint geometry models, we use static GNSS data from AC12. There were two other GNSS stations in proximity to the site of the Sand Point earthquake: AC28, AB07, but the displacements recorded at those sites are too small to be of use compared to the displacements observed at AC12.

## 2.2 Elementary Gaussian Tsunami Source Inversion

In order to estimate the tsunami source, we follow the method generally described by Tsushima et al. (2009) and as implemented by Lin et al. (2020). We compute the hydrodynamic Green's functions for sea surface deformation unit source areas that roughly surround the strike-slip rupture from the USGS finite fault model (Figure 1). Again, with this method, we side-step any complexities of the tsunami source that may arise due to complex fault geometry, multi-fault ruptures, or other tsunami sources such as landslides. The Green's functions are calculated for a 2-D Gaussian tsunami source with a standard deviation of 5 km and amplitude of 1 m. The spacing between the center of the tsunami sources is 10 km. The Gaussian nature of the tsunami source elements ensures that they overlap at the margins, so that smooth variations of sea surface displacements can be expressed with a discrete sum of sources. We use a total of 428 sources in the inversion. We regularize the inversion with a Tikhonov operator of zeroth order and then employ a L-curve criterion from the inversions to find the right level of trade-off between smoothing and misfits of the inversion (Figure S1). The distribution of the tsunami source elements is shown in Figure S2. Green's functions for the two Alaskan tide gauges and four DART buoys were computed for each tsunami source. They were later used for inversion and forward modeling of the tsunami. DART buoy data is produced by a bottom pressure recorder. Seismic arrivals, such as Rayleigh waves and acoustic phases, introduce pressure signals which do not reflect tsunami energy. As a result it is important to mask out these spurious signals and use only the portions that reflect the tsunami itself. At DART station 46403 the tsunami's arrival occurred while seismic/acoustic signals were still visible and could not be used in the inversion. For the tide gauges it has been shown that only the first ~1-1.5 wavelengths can be reliably inverted with later arrivals being difficult to account for in linear inversions (Melgar & Bock, 2013; Yue et al., 2015); as a result we used only the first arriving signals in the inversion. Figure 3 shows as shaded gray regions which time intervals of the water-level data were used in the inversion. The resulting sea surface deformation model was denoised by the method described in Text S1.

## 2.3 Slip Inversion with Hydrodynamic and Geodetic Data

Finally, to test whether the deformation field implied by the geodetic and water level data can be attributed to the co-seismic slip along the strike-slip geometry and/or the megathrust geometry, we perform kinematic and static slip inversions. We jointly invert the DART, tide gauges, and static deformation data on the same strike-slip fault geometry as the USGS finite fault using the MudPy suite of codes (Melgar & Bock, 2015). To explore if megathrust activation is necessary to recreate tsunami waveforms, we also run a joint inversion with this strike-slip and megathrust geometry used by Crowell & Melgar (2020) for the Simeonof earthquake. This later fault has an extent that easily exceeds the limits of the Sand Point rupture; we exclude subfaults near the trench and toe of the slab because the results from 2.2 show that little to no deformation occurs in this region compared to other parts of the slab. As in the hydrodynamic inversion, the slip inversion is regularized using a zeroth order Tikhonov approach and the optimal regularization parameter is obtained from the L-curve criterion. The weighting scheme for the geodetic and water level data uses specific weights to focus more on the linear portion of the waveform data as described by Melgar et al. (2016).

After initial tests we found that the water level data fits improved significantly if the initiation point of the megathrust slip was away from the intersection point with the strike-slip fault and if the rupture propagation speed of the megathrust was comparatively slow. In order to systematically test whether this was really required by the data we ran several different inversions with different rupture speeds and 10 different megathrust slip nucleation points. 3 of the nucleation points are to the west of the strike-slip fault, 3 are along the intersection with the strike-slip fault, and 3 to the east of it. In order to calculate how long to delay rupture along the megathrust, we assume that triggering of the megathrust would be affected by Vs of 3.0 km/s, we compute the distance from the strike-slip hypocenter to each nucleation point and delay it's onset based on that assumed Vs. Once the megathrust begins to slip, we tested 4 rupture speeds: 0.50, 0.70,1.00 and 1.50 km/s. We calculate the RMSE for each combination of nucleation point and rupture speed based on the RMSE and inversion weights used for all stations used in the slip inversion method minus King Cove. We do not include King Cove since, as will be discussed, it routinely does not fit the inversions and, the hydrodynamic inversion suggests that it can be explained by some non-tectonic source. Therefore, it is disqualified from inclusion when assessing the RMSE of the joint inversions.

# 3. Results & Discussion

## 3.1 Forward Tsunami Modeling based on the USGS-NEIC Finite Fault

We calculate the tsunami model based on the vertical deformations from the USGS-NEIC finite fault model to test whether it can explain the tsunami on its own without need for inverting for co-seismic slip along the megathrust. Figure 2 shows the expected pattern from the USGS model and fits to the water level data using it as an initial condition. The expected deformation is much smaller compared to the inversion results of the hydrodynamic and slip methods with peak subsidence of 0.23 m and peak uplift of 0.39 m. Upon visual inspection of Figure 2, it is evident that the sea surface deformation produced by these rupture scenarios is insufficient. Additionally, the tsunami arrives ~1 hour too early at the Sand point tide gauge and has too low a maximum amplitude (trough-to-crest) at ~0.4m compared to the actual 1.32 m at that same site. These findings strongly suggest that a strike-slip earthquake by itself is insufficient to reproduce the tsunami waveforms.

## 3.2 The Hydrodynamic Inversion Method

We find that by inverting only the water level data, for the stations in gray as seen in Figure 3, that we are able to fit the tsunami waveforms very well. We seem to be able to resolve the DARTs and tide gauges' first arrivals almost exactly. Additionally, the model can recreate the far field tsunami waveforms at Hilo and Kawaehai in Hawai'i. It is of note that the primary sea surface deformation signal appears to be trench-parallel (Figure 3). We find almost no indication of what would be expected for strike-slip faulting induced deformations. We note that this does not mean there is no strike-slip faulting. Checkerboard tests of the hydrodynamic inversion reveal that the resolution is not high across the inversion area, so some smearing is to be expected, especially in the regions of smaller signals (Fig. S5). Finally, we find that the trench-parallel deformations fits remarkably well with the rupture zones from the Simeonof and Chignik earthquakes, being bounded to the north and east, respectively, by both earthquakes.

Before we invert both the water level and GNSS data, we check to see what tsunami source is required by only the water level data. This check serves as a diagnosis as to whether any more fault geometries are necessary besides that from the USGS-NEIC finite fault model. The advantages of this model are that it can diagnose areas that potentially may be non-tectonic in origin in addition to tectonic sources. The disadvantage is that the resolution is dominated by whatever is producing large signals. Figure 3 shows that the water level data predominately requires apparent trench-parallel deformations. The amount of vertical deformations necessary to produce such signals is larger at 1.41 m compared to 0.39 m produced by the USGS-NEIC strike-slip solution. It does, however, a much better job of fitting the observed tsunami waveforms (Fig 3).

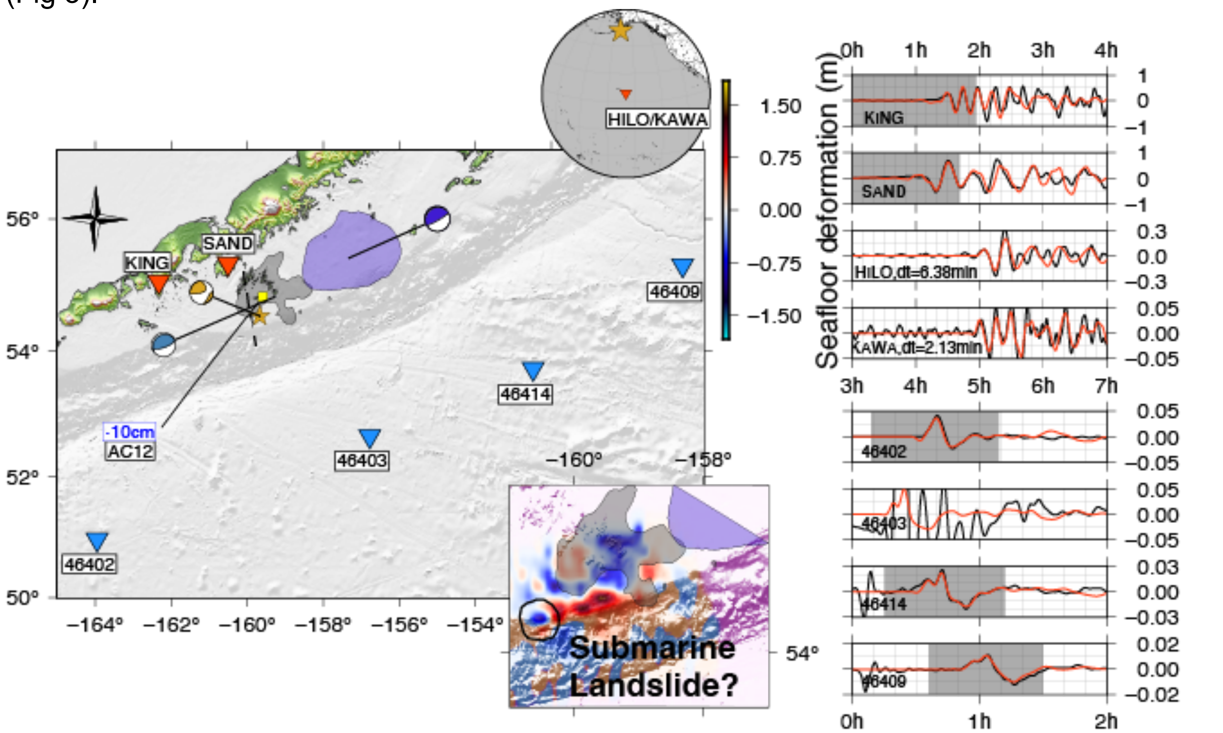


*Figure 3. The hydrodynamic model results. The inset shows a close up of the model result. The black outline denotes an area where a suspected submarine landslide may have occurred based on the classic dipole sea surface deformation pattern. The dashed line is the surface trace for the W-Phase nodal planes used in the USGS finite fault model. The black tsunami waveforms are the 1 min observed data, and the red ones are the simulation results from the sea surface deformation model. Gray boxes outline which portions of the tide gauges and DARTs were used in the tsunami inversion scheme. We shifted the simulated tsunami waveforms for Hilo by 6.38 min and Kawaehai by 2.13 min to match the observed data at the tide gauges*.

## 3.3 Strike-Slip Only Slip Inversion

Before inverting along the megathrust geometry, we again test to see if the strike-slip geometry can reproduce the tsunami and GNSS waveforms. Figure 4 shows two slip models. First, one where the magnitude is limited to that derived from the USGS-NEIC finite fault (Mw 7.57). Here, the tsunami waveform fits have an RMSE 1.818 m while the fit to the coseismic deformation measured by GNSS is good. When we release the magnitude constraint to attempt to fit the tsunami waveforms, the improvement is marginal. Even with an Mw 7.97 earthquake the tsunami waveform fits have an RMSE of 2.063 m and the coseismic deformation fit begins to degrade. This leads us to conclude that the strike-slip geometry alone, like in the hydrodynamic inversion, is not enough to produce the observed waveforms.

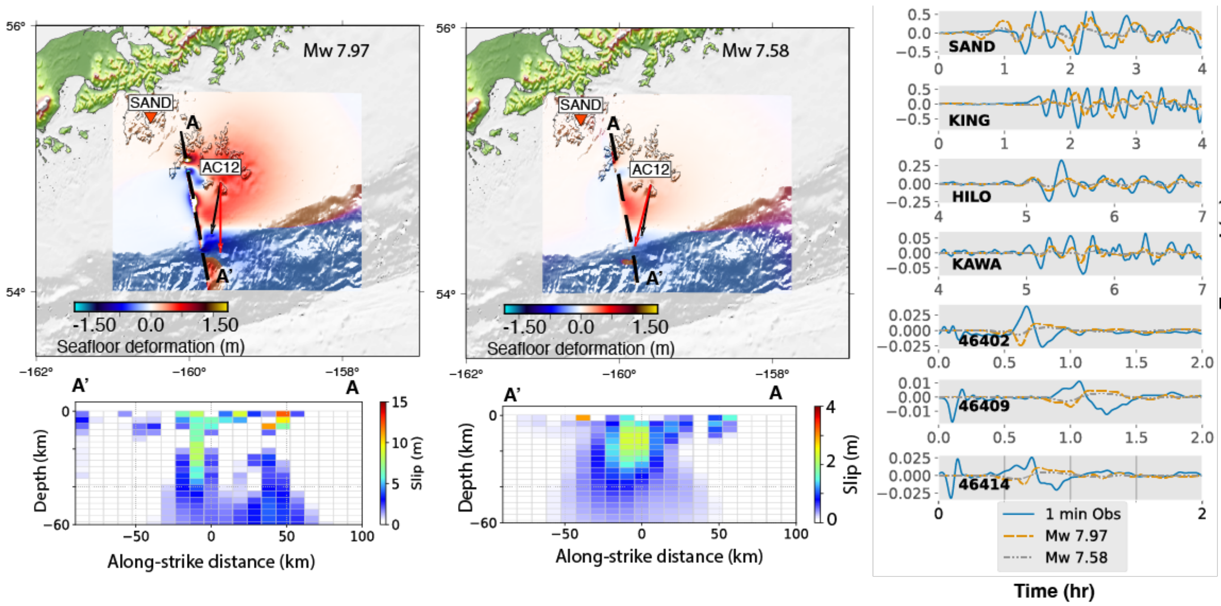


*Figure 4. The fault rupture inversion method results for a strike-slip geometry based off of the USGS-NEIC W-phase solutions. a.) Shows the results for a Mw 7.97. A cross section shows the modeled slip distribution. b.) Shows the results for a Mw 7.58. A cross section shows the modeled slip distribution. The modeled tsunami waveforms are shown in c.).*

## 3.4 Joint Strike-Slip and Megathrust Slip Inversion

In an attempt to make the observations and models parsimonious, we now test including some co-seismic slip along the megathrust interface. We know, at a minimum, that it must be included in any tests we run. We ran two different instances of this strike-slip plus megathrust inversion. Because tsunami propagation speeds are significantly slower than common earthquake rupture speeds, instantaneous ruptures are usually sufficient to recreate hydrodynamic data (e.g. Williamson et al., 2019). So, we first test to see if a static instantaneous rupture of both the strike-slip and megathrust interface at the same time can explain the waveforms. Next, we test whether delaying the megathrust slip (due to either static or dynamic triggering) and allowing it to slip with a finite duration is needed and explore a range of different rupture speeds.

The results of these tests can be seen on Figures 5 & 6 (vertical deformations can be seen in Figure S6). The strike-slip rupture velocity was held to 3.0 km/s in an attempt to help recreate the tsunami waveform data at DARTs 46414 and 46409. We test static and dynamic triggering at 10 nucleation points in the rupture area. We observe that static triggering, which in this case refers to simultaneous rupture start along both the strike-slip and megathrust, does not explain the waveforms as well as certain nucleation points, which leads to the potentiality that the megathrust co-seismic slip initiates some time after the initiation of the strike-slip earthquake. From Figure 5, We find that the minimum RMSE misfit occurs for a megathrust rupture velocity of 1.0 km/s nucleating at nucleation point 3 29.5 s after the strike slip hypocenter. We note that the megathrust co-seismic slip appears to be roughly bounded by Simeonof to the north and Chignik to the east in these results as well (Figure 6). From this location along the megathrust, the rupture front propagates from the SW to the NE of the proposed rupture domain. The inversion's ability to resolve co-seismic slip along the megathrust is greatest the closer it is to the strike-slip plane (Figure S7). We note that the co-seismic slip is underpredicted near it, and that co-seismic slip is smoothed out near the edge of the inversion area. The ability to resolve co-seismic slip along the strike-slip plane is limited to the areas immediately close to AC12.

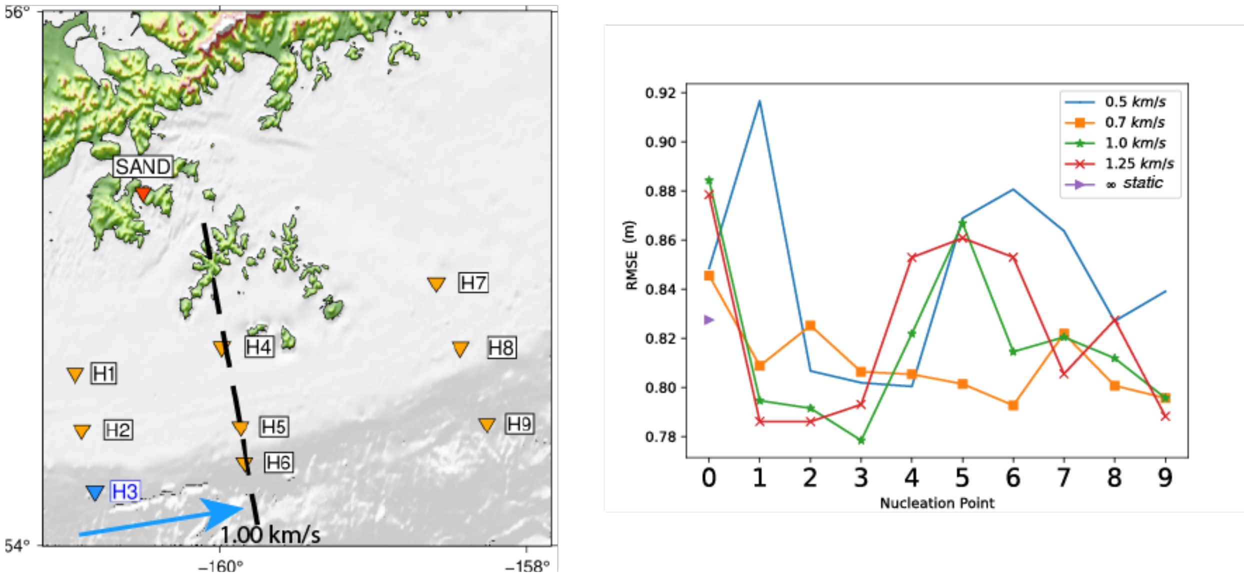


*Figure 5. 9 different megathrust nucleation points that are used to gauge the sensitivity of the tsunami and geodetic waveforms at 4 different rupture velocities: 0.50 km/s, 0.70 km/s, 1.00 km/s and 1.25 km/s. Hypocenter 3 is shown in blue in a.) along with the direction and speed of propagation. b.) The RMSEs of the four different rupture speeds and the static triggering at nucleation point 0 are shown. The RMSEs are shown for each rupture speed at each nucleation point. Nucleation point 0 is the hypocenter as derived from the USGS-NEIC model, see Figure 2.*

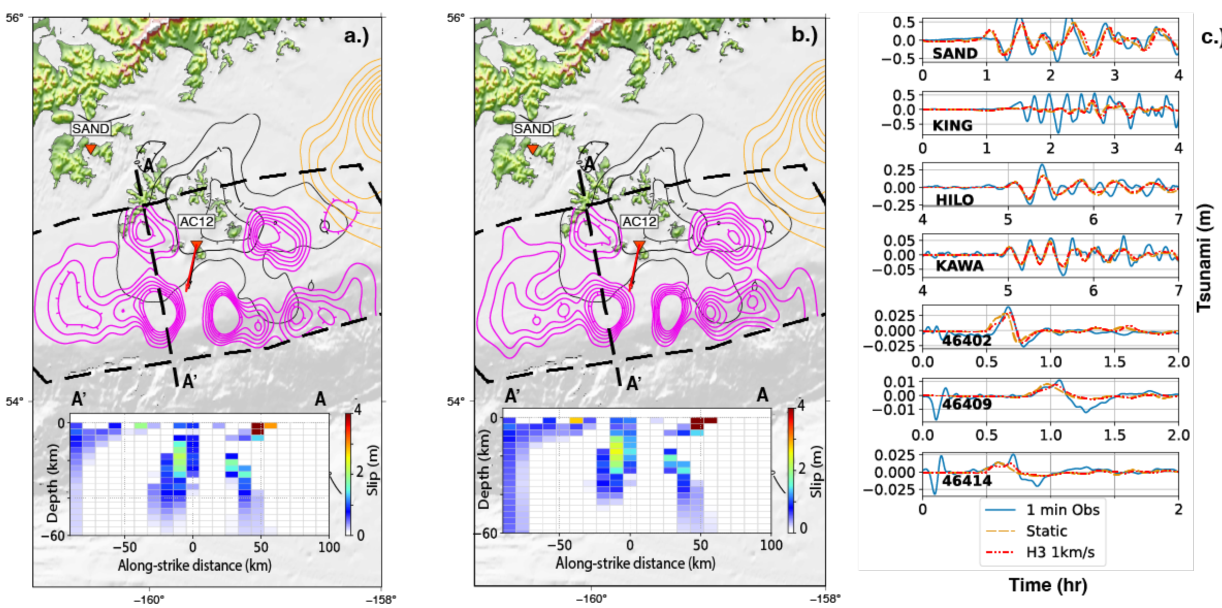


*Figure 6. a.) The kinematic co-seismic slip is centered at nucleation point 3 with a rupture velocity of 1.00 km/s along the megathrust and 3.00 km/s along the strike-slip. A-A' is the strike-slip plane from the NEIC W-phase. The slip distribution is shown. b.) The static vertical deformation is centered on the hypocenter from the W-phase solution. The rupture speed is 1.25 km/s for the megathrust and 3.00 km/s for the strike-slip. c.) The tsunami waveforms for the vertical*

*deformations seen in a.) and b.). The contour spacing for the three distributions of contours is 0.5 m.*

## 3.5 Potential Submarine Landslide

The addition of a megathrust co-seismic slip produces a significant improvement in the waveform fits compared to the strike-slip fault alone and the GNSS static offset. However, one piece of data remains problematic. The King Cove tide gauge (Fig. 1) recorded >30 cm tsunami wave amplitudes. Neither the strike-slip only or joint megathrust inversions can recreate the tsunami waveforms at that location; they are consistently underestimated (Figures 4,5). Meanwhile, in the hydrodynamic inversion (Figure 2), which is sensitive to both tectonic and non-tectonic tsunami sources, King Cove is fit well. We find that a specific section of the hydrodynamic inversion result from Figure 3 is needed to aid in recreating the tsunami waveform. In this particular area, the vertical deformation has an apparent submarine landslide signal. Landslides typically produce a positive-negative dipole of sea-surface deformation. The negative portion (subsidence) corresponds to the area where mass is removed, while the positive lobe corresponds to the area where the excavated mass moves downslope (e.g. WIlliamson et al., 2020). The location of such a dipole signal and a potential landslide is highlighted in Fig. 3. This area is on the steep section of the shelf-break and is within 20 km of the ALEUT-05 active source survey (Bécel et al, 2017). That study noted widespread evidence that this part of the continental slope is prone to submarine landslides. Further the potential landslide highlighted in Fig. 3 has the expected positive-negative dipole sea surface deformation pattern expected for a submarine landslide (e.g. Williamson et al.,2020). Thus, the potential of submarine landslides contributing to the tsunami waveforms is considerably high, especially since something in this area is needed to explain the tsunami waveforms at King Cove. If we add that landslide source to the joint strike-slip and megathrust geometry, we obtain the tsunami fits observed in Fig. 7. It should be noted that we add the submarine landslide as if it occurs instantaneously 140 s after the earthquake begins on the strike-slip component. The degradation of fits to 46402 shows the limitations of such an assumption. Likely, if it is indeed a submarine landslide, it occurred over many seconds. Modeling of a landslide in an already complex earthquake source is difficult and the subject of future work.

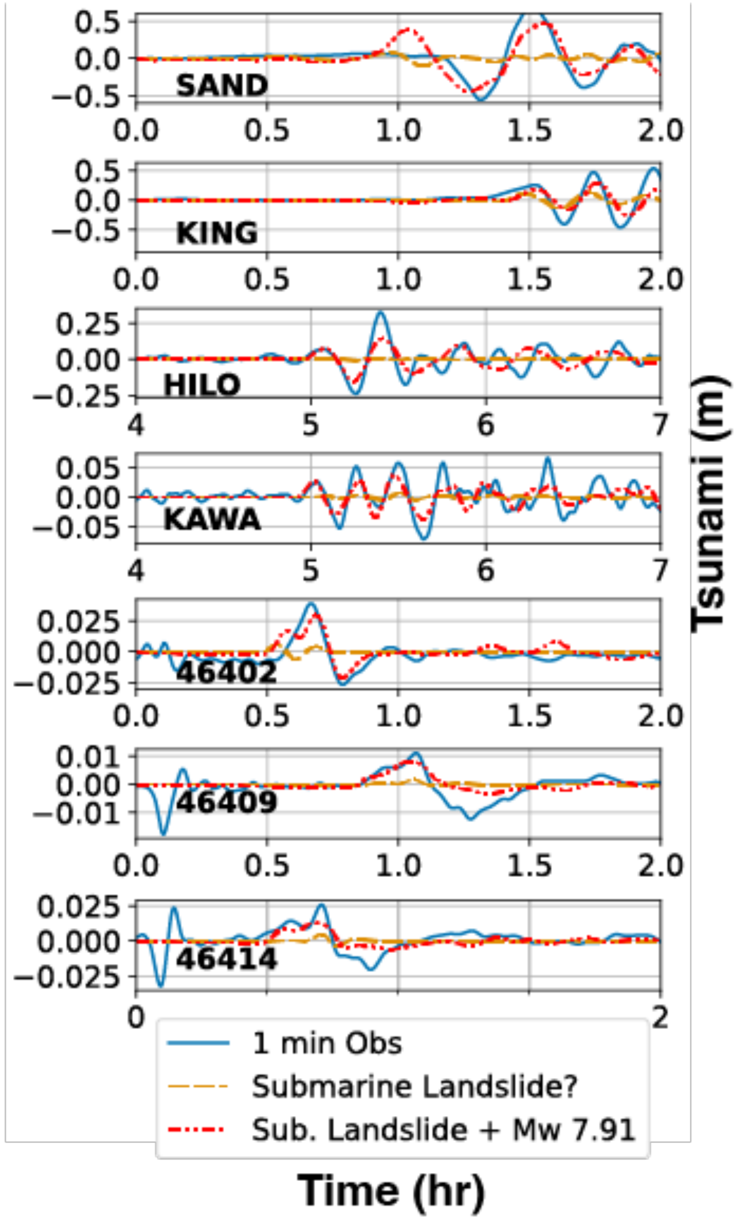


*Figure 7. The tsunami waveforms from the potential submarine landslide location denoted by the black outline in Figure 3. The modeled earthquake that was added to the potential submarine landslide is the result from hypocenter 3 with a rupture velocity of 1.00 km/s.*

## 3.6 Implications

The hydrodynamic and slip inversions imply that potentially large amounts of megathrust slip went undetected, or at least unmodeled by far-field seismic data and products produced shortly after the Sand Point earthquake. However, this slip seems to be required by both inversion methods. We cannot at present resolve the issue of how such a large quantity of slip would go undetected and we recognize that it is an outstanding challenge for the Sand Point earthquake. We posit that the megathrust component of the Sand Point earthquake slips in such a way that it radiates inefficiently. Coupled with a potentially energetic strike-slip rupture happening concurrently, the megathrust component of the event could have been obscured by it. This has recently been observed in other complex earthquakes, most notably the 2021 Sandwich islands sequence where multiple large, complex events occuring in close spatiotemporal proximity lead to far-field teleseismic magnitudes smaller than the aggregate events and complex focal mechanisms (Jia et al., 2021)

It has been noted that near-trench “tsunami earthquakes" rupturing through the shallow low rigidity portions of the megathrust can have this feature (e.g. Satake & Tanioka, 1999) and are depleted of both far-field (Newman et al., 2012) and near-field (Sahakian et al., 2020) seismic radiation. A characteristic of these is very slow rupture (e.g., Riquelme & Fuentes, 2021). Our slip inversion results do suggest that a slow rupture speed for the megathrust ,~1 km/s, improves the data fits globally. Meanwhile, our hydrodynamic inversion results were unable to suggest if slow rupture velocities were present in the event (Figures S8-13). However, regional intensities were not anomalously low for an M7.6, nor was far field radiated energy, whether this is because the strike-slip fault radiated with the usual efficiency, obscuring the inefficient megathrust process remains to be addressed.

So, even though there is evidence for this slow rupture we note that the sensitivity of tsunami data to this aspect of source kinematics is limited (e.g. Williamson et al., 2019). This is due to tsunami propagation speeds traditionally being much slower than rupture speeds. However, as rupture speeds get particularly slow <1km/s this sensitivity increases (Riquelme et al., 2020). Nonetheless, this reduced resolution makes it difficult to interpret whether all the features of the megathrust slip are needed by the data, particularly the slip patches that “re-rupture” regions that slipped in previous events. Indeed, the predicted vertical deformation from the joint strike-slip megathrust rupture (Figure 8) resemble that from the hydrodynamic inversion (FIgure 3) but it's not an exact match and the fits to the water-level data are lower.

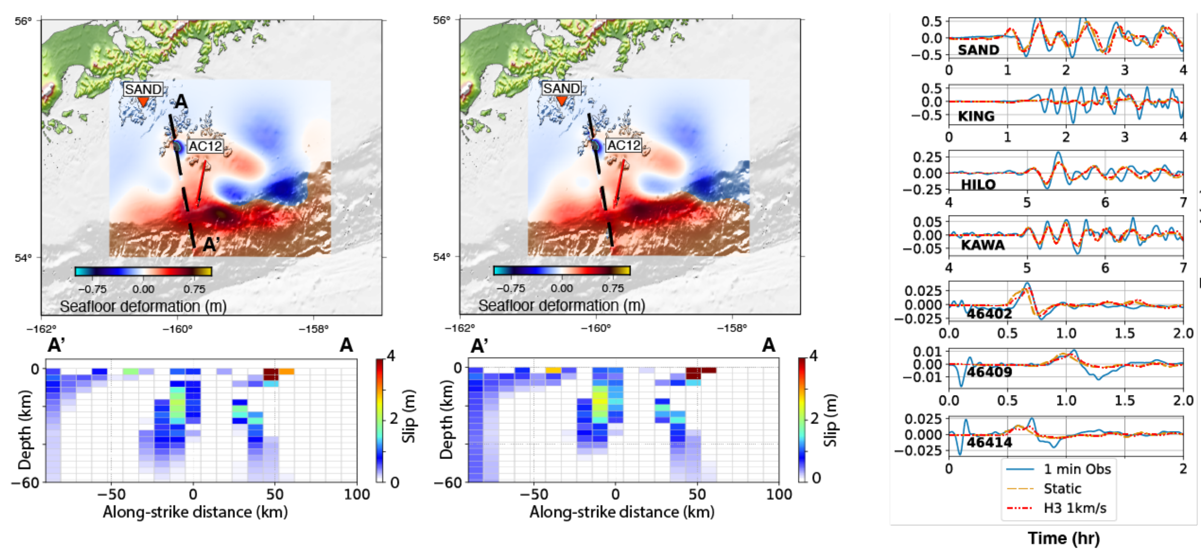


*Figure 8. a.) The kinematic vertical deformation is centered at nucleation point 3 with a rupture velocity of 1.00 km/s along the megathrust and 1.50 km/s along the strike-slip. A-A' is the strike-slip plane from the NEIC W-phase. The slip distribution is shown. b.) The static vertical deformation is centered on the hypocenter from the W-phase solution. The rupture speed is 1.5 km/s for each geometry. c.) The tsunami waveforms for the vertical deformations seen in a.) and b.).*

Another possibility discussed by Ma & Nie (2019) is that the rupture progresses at a more “traditional” speed.This would make sense since most of the Shumagin segment is imaged to be mostly creeping in the interseismic period (Li & Freymueler, 2018) and thus can reasonably be inferred to prefer rate-strengthening modes of rupture. Indeed (Crowell & Melgar, 2020), imaged some afterslip in this portion of the megathrust. In this model the megathrust slip during the Sand Point earthquake would be a peculiar kind of “fast" slow-slip. The rupture front propagates at a traditional speed, near shear-wave speeds, but once slip starts it is very slow. These processes would ostensibly be enough to keep the true extent of the megathrust co-seismic slip ‘silent’ in the seismic data. Moreover, the Mw 8.6 1946 earthquake on the neighboring Sanak segment was highly deficient in seismic radiation, with a teleseismic magnitude of only 7.4, indicating there may be some structural control on the megathrust that generates slow and long ruptures devoid of seismic radiation (Lopez & Okal, 2006). In the present work we cannot resolve these nuances, which have important implications for the geodynamics of the megathrust, but suggest that, at a minimum, if the megathrust was involved, and it seems like this is needed to reconcile, at least in part, the tsunami observations, that slip on it propagated slowly. Future work to clarify this is to produce a kinematic model that includes all regional observations, including strong motion, HR-GNSS, and far field data to systematically test whether such joint multi-fault models with complex kinematics can be invoked to account for all the geophysical observables.

Co-seismic slip along the megathrust propagating from the NW to NE of the proposed rupture area would have the Sand Point rupture arresting at the boundary of the July 2021 Chignik earthquake (Fig. 6). To what extent Sand Point plays a role in the triggering of Chignik is uncertain and outside the scope of this paper. We do find that the sea surface deformations do have the appearance of being bounded to the north and east by the rupture zones of the Simeonof and Chignik rupture zones (Figure 3). It is something that needs to be further investigated. The reconciled magnitude of the earthquake from the hydrodynamic inversion method and the joint geometry fault rupture inversion method is Mw 7.91 ($M_0$ = $1.80 \times 10^{20}$ N-m). The magnitude of the strike-slip segment is Mw 7.44 ($M_0$ = $9.22 \times 10^{20}$ N-m). The Mw for the megathrust is Mw 7.85 ($M_0$ = $7.43 \times 10^{20}$ N-m). Xiao et al. (2021) find that the amount of slip deficit left to rupture after the Simeonof earthquake, updip of the rupture zone (Figure 7 of Xiao et al. (2021)),is equivalent to a Mw 7.8. The majority of the proposed modeled megathrust co-seismic slip for the Sand Point event falls between 32 km down-dip to ~15 km up-dip of the megathrust. Crowell and Melgar (2020) along with Liu et al. (2020) and Xiao et al. (2021) have found that the Simeonof earthquake ruptured ~35 km up-dip. If this is indeed the case, then it is likely that activation along the megathrust potentially exhausted accumulated slip in this region of the Shumagin Gap. However, we note that the co-seismic slip in our models does not extend up-dip of 15 km. There is also some limited overlap in our model of the Sand Point earthquake with the earlier Simeonof slip, to what extent this is required will also be important to determine with a more comprehensive kinematic slip inversion. Checkerboards (Figs S6 and S7) find that this portion of the inversion is resolved well in the hydrodynamic model but that there is also appreciable smearing in the slip inversion. So, whether the un-ruptured sections of the Shumagin segment will experience post-seismic relaxation, leading to decreased hazards, or continue to be coupled and a source of future tsunamigenic events to the Aleutian communities in this region is uncertain.

Herman & Furlong (2021) show that spatial variations in displacements caused by coupling between the overriding plate and slab in the 1938 asperity and low coupling throughout the Shumgain segment would likely cause large, right-lateral shear stresses in the section of the segment that produced the strike-slip component of the earthquake. The presence of a strike-slip plane may lead to helpful hints about the state of locking in this region of the megathrust. We posit that the dynamic triggering of nucleation point 3 by the strike-slip component of the earthquake occurred in a region of low coupling (Li & Freymueller, 2018). The low coupling would allow for shear waves to cause displacements large enough to promote rupture in this region. The rupture front would then propagate to the NW into a region of potentially higher coupling and higher slip deficits where it would eventually stop (Li & Freymueller, 2018; Xiao et al., 2021). This interpretation is thought to be more likely given the nature of the location of nucleation point 3 and those in the western portion of the model domain. More work would be needed to provide solid reasoning for why this result would be the case.

Finally, whether it truly is a submarine landslide(s) that aides in generating the tsunami waveforms at King Cove needs to be further explored perhaps by repeated multibeam bathymetry surveys. If there have been significant changes, then it may potentially provide solid footing for what the inversion methods are elucidating. If not, then other features would have to be explored to explain the tsunami signal at King Cove. More data is ultimately needed to further constrain the inversion results from the fault rupture inversion method. One static GNSS station is used due to the large signals seen at that site. We do not use other GNSS stations in an attempt to avoid overfitting of the geodetic data. Seafloor GNSS stations were in deployment during the time of the Sand Point earthquake; however, those data are currently unavailable, but may prove to be critical constraints for a rupture inversion.

# 4. Conclusion

We have shown that strike slip models for the 2020 Sand Point earthquake event are inadequate for generating the observed tsunami. Using water level inversion techniques and fault rupture inversion method we find that there was potentially a co-seismic slip along the megathrust during the October 19, 2020 Sand Point strike-slip earthquake. The sea surface deformation necessary to recreate the tsunami waveforms at the Alaskan and Hawaiian tide gauges as well as the DART buoys requires it. Slip on both the strike-slip fault and the megathrust is equivalent to a Mw 7.91. We find that a slow rupture propagation speed of 1 km/s potentially does explain the observations well so we posit that the megathrust slip does not contribute much seismic radiation, perhaps due to slow slip rates during rupture. The rupture front propagates at this speed from nucleation point 3 into a region of high slip deficit updip of the July rupture zone but does not slip updit of the depths at ~15 km. We have shown that the nucleation of rupture at this point occurs 29.5 s after the strike-slip rupture initiates, potentially from that rupture's shear waves. We have also shown that a submarine landslide is potentially necessary to explain the tsunami waveforms at King Cove, in addition to the potential co-seismic megathrust.

# Data Availability Statement

The water level data for the DART buoys can be obtained from the DART website (https://www.ndbc.noaa.gov/dart.shtml), for the tide gauges it can be obtained from NOAA's CO-OP the Environmental Research Division's Data Access Program (ERDDAP) server (https://opendap.co-ops.nos.noaa.gov/erddap/index.html), the vertical offset for AC12 was obtained from the Nevada Geodetic Laboratory website (http://geodesy.unr.edu/PlugNPlayPortal.php). The water level inversion code is available from Github (https://github.com/ssantellanes/water-level-inversion) and archived on Zenodo at

Santellanes et al. (2021). The static slip inversions were generated using the FakeQuakes code which is part of the MudPy source modeling toolkit available on GitHub (https://github.com/dmelgarm/MudPy), the latest version is archived on Zenodo at Melgar (2021).

# Acknowledgments

We'd like to thank Rich Briggs, Ben Brooks, Dara Goldberg, and Rob Witter for their discussion of Alaskan earthquakes. This work was partially funded by NASA grants # 80NSSC19K0360 and 80NSSC19K1104.

# References

Abers, G. A. (1992). Relationship between shallow- and intermediate-depth seismicity in the Eastern Aleutian Subduction Zone. *Geophysical Research Letters*, *19*(20), 2019–2022. Retrieved from https://doi.org/10.1029/92GL02060

Bécel, A., Shillington, D. J., Delescluse, M., Nedimović, M. R., Abers, G. A., Saffer, D. M., et al. (2017). Tsunamigenic structures in a creeping section of the Alaska subduction zone. *Nature Geoscience*, *10*(8), 609–613. https://doi.org/10.1038/NGEO2990

Blewitt, G., W. C. Hammond, and C. Kreemer (2018), Harnessing the GPS data explosion for interdisciplinary science, Eos, 99, https://doi.org/10.1029/2018EO104623

Crowell, B. W., & Melgar, D. (2020). Slipping the Shumagin Gap: A Kinematic Coseismic and Early Afterslip Model of the Mw 7.8 Simeonof Island, Alaska, Earthquake. *Geophysical Research Letters*, *47*(19), 1–7. https://doi.org/10.1029/2020GL090308

Davies, J., Sykes, L., House, L., & Jacob, K. (1981). Shumagin Seismic Gap, Alaska Peninsula: History of Great Earthquakes, Tectonic Setting, and Evidence for High Seismic Potential. *Journal of Geophysical Research*, *86*, 3821–3855.

Elbanna, A., Abdelmeguid, M., Ma, X., Amlani, F., Bhat, H. S., Synolakis, C., & Rosakis, A. J. (2021). Anatomy of strike-slip fault tsunami genesis. *Proceedings of the National Academy of Sciences*, *118*(19).

Fukao, Y. (1979). Tsunami earthquakes and subduction processes near deep-sea trenches. *Journal of Geophysical Research: Solid Earth*, *84*(B5), 2303–2314. https://doi.org/10.1029/JB084iB05p02303

Jia, Z., Zhan, Z., & Kanamori, H. The 2021 South Sandwich Island Mw 8.2 earthquake: a slow event sandwiched between regular ruptures (pre-print).

Goldberg, D. E., Melgar, D., Sahakian, V. J., Thomas, A. M., Xu, X., Crowell, B. W., & Geng, J. (2020). Complex rupture of an immature fault zone: A simultaneous kinematic model of the 2019 Ridgecrest, CA earthquakes. Geophysical Research Letters, 47(3), e2019GL086382.

Hayes, G. P. (2017). The finite, kinematic rupture properties of great-sized earthquakes since 1990. *Earth and Planetary Science Letters*, *468*, 94-100.

Hayes, G. P., Moore, G. L., Portner, D. E., Hearne, M., Flamme, H., Furtney, M., & Smoczyk, G. M. (2018). Slab2, a comprehensive subduction zone geometry model. *Science*, *362*(6410), 58-61.

Herman, M. W., & Furlong, K. P. (2021). Triggering an unexpected earthquake in an uncoupled subduction zone. *Science Advances*, *7*(13), 1–10. https://doi.org/10.1126/sciadv.abf7590

Kanamori, H., & Kikuchi, M. (1993). the 1992 Nicaragua Earthquake. *Nature*, *361*(February), 714–716.

Larson, K. M., Lay, T., Yamazaki, Y., Cheung, K. F., Ye, L., Williams, S. D. P., & Davis, J. L. (2020). Dynamic Sea Level Variation from GNSS: 2020 Shumagin Earthquake Tsunami Resonance and Hurricane Laura. *Geophysical Research Letters*. https://doi.org/10.1029/2020gl091378

Lay, T., Kanamori, H., Ammon, C. J., Koper, K. D., Hutko, A. R., Ye, L., et al. (2012). Depth-varying rupture properties of subduction zone megathrust faults. *Journal of Geophysical Research: Solid Earth*, *117*(4), 1–21. https://doi.org/10.1029/2011JB009133

LeVeque, R. J., George, D. L., & Berger, M. J. (2011). Tsunami modelling with adaptively refined finite volume methods. *Acta Numerica*, *20*, 211-289.

Li, S., & Freymueller, J. T. (2018). Spatial Variation of Slip Behavior Beneath the Alaska Peninsula Along Alaska-Aleutian Subduction Zone. *Geophysical Research Letters*, *45*(8), 3453–3460. https://doi.org/10.1002/2017GL076761

Lin, J. T., Aslam, K. S., Thomas, A. M., & Melgar, D. (2020). Overlapping regions of coseismic and transient slow slip on the Hawaiian décollement. *Earth and Planetary Science Letters*, *544*, 116353. https://doi.org/10.1016/j.epsl.2020.116353

Liu, C., Lay, T., Xiong, X., & Wen, Y. (2020). Rupture of the 2020 MW 7.8 Earthquake in the Shumagin Gap Inferred From Seismic and Geodetic Observations. *Geophysical Research Letters*, *47*(22), 1–9. https://doi.org/10.1029/2020GL090806

Ma, S., & Nie, S. (2019). Dynamic wedge failure and along arc variations of tsunamigenesis in the Japan trench margin. Geophysical Research Letters, 46(15), 8782-8790.

Melgar, D., & Bock, Y. (2013). Near-field tsunami models with rapid earthquake source inversions from land- and ocean-based observations: The potential for forecast and warning. *Journal of Geophysical Research: Solid Earth*, *118*(11), 5939–5955. https://doi.org/10.1002/2013JB010506

Melgar, D., & Bock, Y. (2015). Kinematic earthquake source inversion and tsunami runup prediction with regional geophysical data. *Journal of Geophysical Research: Solid Earth*, 120(5), 3324-3349.

Melgar, D., Fan, W., Riquelme, S., Geng, J., Liang, C., Fuentes, M., ... & Fielding, E. J. (2016). Slip segmentation and slow rupture to the trench during the 2015, Mw8. 3 Illapel, Chile earthquake. Geophysical Research Letters, 43(3), 961-966.

Melgar, D. (2021). dmelgarm/MudPy: v1.3. Zenodo. doi:10.5281/zenodo.5397091

Okal, E. A., & Synolakis, C. E. (2003). A theoretical comparison of tsunamis from dislocations and landslides. *Pure and Applied Geophysics*, *160*(10–11), 2177–2188. https://doi.org/10.1007/s00024-003-2425-x

Pasyanos, M.E., T.G. Masters, G. Laske, and Z. Ma (2014). LITHO1.0: An updated crust and lithospheric model of the Earth, J. Geophys. Res., 119 (3), 2153-2173, DOI: 10.1002/2013JB010626.

Riquelme, S., Schwarze, H., Fuentes, M., & Campos, J. (2020). Near-field effects of earthquake rupture velocity into tsunami runup heights. Journal of Geophysical Research: Solid Earth, 125(6), e2019JB018946.

Riquelme, S., & Fuentes, M. (2021). Tsunami Efficiency Due to Very Slow Earthquakes. *Seismological Research Letters*. https://doi.org/10.1785/0220200198

Sahakian, V. J., Melgar, D., & Muzli, M. (2019). Weak near-field behavior of a tsunami earthquake: Toward real-time identification for local warning. Geophysical Research Letters, 46(16), 9519-9528.

Santellanes, S.R., Lin, J.T., & Melgar, D.. (2021, September 9). ssantellanes/water-level-inversion: First release (Version v1.0.0). Zenodo. https://doi.org/10.5281/zenodo.5498175

Satake, K., & Tanioka, Y. (1999). Sources of Tsunami and Tsunamigenic Earthquakes in Subduction Zones. *Pure and Applied Geophysics*, *154*, 467–483. https://doi.org/10.1007/978-3-0348-8679-6_5

Titov, V. V., González, F. I., Bernard, E. N., Eble, M. C., Mofjeld, H. O., Newman, J. C., & Venturato, A. J. (2005). Real-time tsunami forecasting: Challenges and solutions. *Natural Hazards*, *35*(1), 41–58. https://doi.org/10.1007/s11069-004-2403-3

Tsai, V. C., Ampuero, J. P., Kanamori, H., & Stevenson, D. J. (2013). Estimating the effect of Earth elasticity and variable water density on tsunami speeds. Geophysical Research Letters, 40(3), 492-496.

Tsushima, H., Hino, R., Fujimoto, H., Tanioka, Y., & Imamura, F. (2009). Near-field tsunami forecasting from cabled ocean bottom pressure data. *Journal of Geophysical Research: Solid Earth*, *114*(6), 1–20. https://doi.org/10.1029/2008JB005988

Williamson, A., Melgar, D., & Rim, D. (2019). The effect of earthquake kinematics on tsunami propagation. Journal of Geophysical Research: Solid Earth, 124(11), 11639-11650.

Witter, R. C., Briggs, R. W., Engelhart, S. E., Gelfenbaum, G., Koehler, R. D., and Barnhart, W. D. (2014), Little late Holocene strain accumulation and release on the Aleutian megathrust below the Shumagin Islands, Alaska, *Geophysical Research Letters*, 41, 2359– 2367, doi:10.1002/2014GL059393.

Xiao, Z., Freymueller, J. T., Grapenthin, R., Elliott, J. L., Drooff, C., & Fusso, L. (2021). The deep Shumagin gap filled: Kinematic rupture model and slip budget analysis of the 2020 Mw 7.8

Simeonof earthquake constrained by GNSS, global seismic waveforms, and floating InSAR. *Earth and Planetary Science Letters*, *576*, 117241.

Ye, L., Lay, T., Kanamori, H., & Rivera, L. (2016). Rupture characteristics of major and great (Mw≥ 7.0) megathrust earthquakes from 1990 to 2015: 1. Source parameter scaling relationships. *Journal of Geophysical Research: Solid Earth*, *121*(2), 826-844.

Yue H., Lay T., Li L., Yamazaki Y., Cheung K.F., Rivera L., Hill E.M., Sieh K., Kongko W., & Muhari, A. Validation of linearity assumptions for using tsunami waveforms in joint inversion of kinematic rupture models: Application to the 2010 Mentawai Mw 7.8 tsunami earthquake. *Journal of Geophysical Research: Solid Earth*. 2015,120(3),1728-47.